DOI: 10.13009/EUCASS2022-6196
9TH EUROPEAN CONFERENCE FOR AERONAUTICS AND SPACE SCIENCES (EUCASS)

Additive manufacturing capabilities for heat switch technology: Key challenges & knowledge gaps

MAŠEK Jakub[1*]
[1] *Brno University of Technology, Institute of Aerospace Engineering, Technicka 2, 61669 Brno, Czech Republic*
* Jakub.Masek@vutbr.cz

LÖFFELMANN František, POPELA Robert, KUBÍK Petr, ŠEBEK František, KOUTNÝ Daniel, MALÝ Martin, PANTĚLEJEV Libor[2], PAMBAGUIAN Laurent[3]

[2] *Brno University of Technology, Faculty of Mechanical Engineering, Technicka 2, 61669 Brno, Czech Republic, Frantisek.Loffelmann@vutbr.cz; popela.r@fme.vutbr.cz; kubik.p@fme.vutbr.cz; sebek@fme.vutbr.cz; Daniel.Koutny@vut.cz; Martin.Maly2@vut.cz; pantelejev@fme.vutbr.cz*

[3] *European Space Agency (ESA - ESTEC), Materials and Processes Section (TEC-MSP), Keplerlaan 1, NL-2200 AG Noordwijk, The Netherlands, Laurent.Pambaguian@esa.int*

Abstract

The paper is to provide an overview of the key challenges and knowledge gaps in additive manufacturing of metals applied to two parts of a novel heat switch technology – a Baseplate and a Flexible thermal structure. Additive design, optimization and manufacturing capabilities as well as quality of produced parts were investigated. The key challenge was to manufacture bio-inspired structure without internal supports and assure 190 surfaces to be in a contact at the same time for efficient heat transfer. Finally, modern trends in additive as multi-material design and manufacturing or effect of defects are discussed for further evolution of parts.

1. Introduction

Additive manufacturing of metals, as a growing market, has a lot to offer in terms of design-manufacturing capabilities and sustainability [1]. Therefore, it attracts key players and entrepreneurs in the space industry to reach better performance of parts at a lower mass. One of the game-changing applications is thermal hardware [2; 3].

Thermal management is an integral part of each spacecraft. It is necessary to ensure the thermal regulation for internal electronics and payload to allow them to work in suitable conditions. A phase change material-based (PCM) heat switch [4; 5] is a one type of many [6; 7] studied in literature. The switch technology can be divided in passive and active devices that differ in temperature and conductivity parameters as well as in the physical principle of function.

Selective laser melting (SLM) technology is a currently leading innovative manufacturing process among the additive technologies that accelerates changes in many engineering areas, particularly the aerospace [8; 9]. Several studies investigated space components optimized and produced by SLM technology from AlSi10Mg powder, as brackets [10; 11], CubeSat frame [12], antennas and waveguides [13] or heat pipes [14]. The benefit of printing the components layer-by-layer enables a different approach in design and manufacturing process. Costs, weight and material wasting can be reduced while producing parts with the same or even better mechanical properties [15; 16]. However, only few additive parts were qualified for space flight [11; 17; 18]. The technology itself creates micro and macro structure defects, porosity, thermal deformations and poor surface quality [19; 20; 21]. Effect of defects [22] and related inspection and post-processing technologies are among the most critical parameters for larger space application and qualification of additive parts. Higher amount of porosity, lower geometry and surface precision are the key disadvantages of aluminium-based materials despite of easier SLM manufacturing and larger knowledge base of material properties [23; 24].

DOI: 10.13009/EUCASS2022-6196

A miniaturized heat switch [25; 26] (Figure 1) is a device under the development dedicated to efficient, autonomous and powerless temperature regulation based on thermo-physical properties of paraffin. The technology repeatedly couples or decouples the heat source with external radiator that dissipates the excess of energy to the environment. It shall have two-position on/off thermal transfer up to 10 W. The switch shall work in deep space and Martian conditions to withstand temperatures from – 125 °C to + 60 °C. The implementation of additive technology is expected to enhance the design towards an operational sample.

The paper is to provide an overview of the key challenges and knowledge gaps in additive SLM manufacturing applied to two parts of the novel heat switch technology – a Baseplate and a Flexible thermal structure. In addition, to provide a context of modern trends in additive for further evolution of parts.

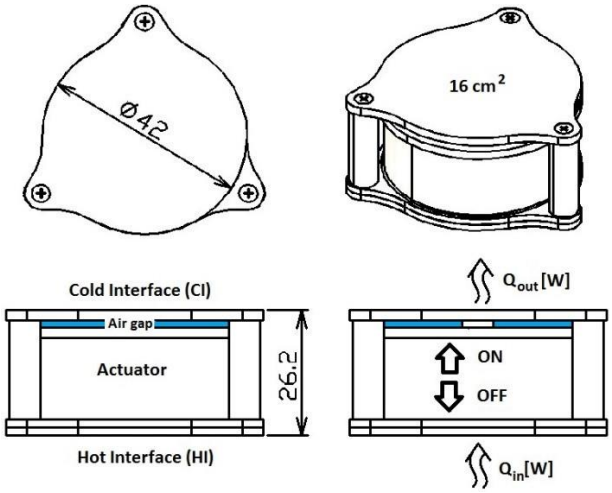

Figure 1: Miniaturized heat switch schema (dimensions in millimetres)

1.1 Legacy issues of parts

Baseplate (BP) part represents a half of paraffin pressure container (Figure 1a). The component (Ø32 mm and 17.6 mm in height) of mass roughly 30 g shall withstand an internal pressure of up to 16 MPa, while the deformations reach less than 0.02 mm. The Baseplate shall allow paraffin melting and on the contrary, prevent its leakage. The flatness of the plate is essential to provide a contact interface to an external heat source for efficient heat transfer. However, paraffin pressure driving the actuator causes in the 'on' mode swelling of the switch so that the contact surface might be significantly reduced (Figure 2b) [26]. The goal is therefore to optimize the thermal-stiffness properties by adding internal reinforcements at a minimum weight.

(a)

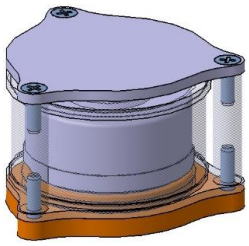

(b)

Temperature of paraffin [°C]	*Paraffin pressure* [MPa]*	*Deflection [mm]*
20	7.8	0.122
40	12.5	0.193
60	16.4	0.251

* MHS internal paraffin pressure was estimated based on the measured deflections; CAD models were analysed by finite element analysis FEA at different loads of paraffin pressure to reach the same deformations.

Figure 2: Baseplate part; (a) former design; (b) temperature-to-deformation dependence based on paraffin pressure

The second part, Flexible thermal structure (FTS), represents the path of heat transfer. The component (Ø56 mm and 24.1 mm in height) of mass roughly 70 g has a two-position on/off mode allowing a vertical linear movement and a thermal conductivity higher than 1.5 $W \cdot K^{-1}$. When the temperature of paraffin rises, the actuator pushes the flexible structure to prolong by 1.7 mm (7.6 %) and creates the heat conductive path.

(a)

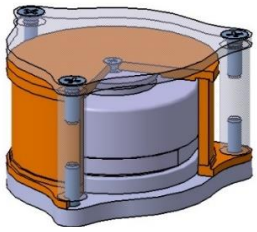

(b)

Parameter	*Current value*	*Requirement*
Thermal conductivity	0.365 $W \cdot K^{-1}$	> 1.5 $W \cdot K^{-1}$
FTS weight (*3-parts assembly*)	55.1 g	< 55.1 g
Specific thermal ratio	6.6 $W \cdot K^{-1} \cdot kg^{-1}$	> 27.2 $W \cdot K^{-1} \cdot kg^{-1}$

Figure 3: Flexible thermal structure; (a) former design; (b) design parameters

The Flexible structure (Figure 3a) was initially made of copper braid soldered to two copper plates. However, the welded joint and the copper braid proved to be unacceptable. A micro-computed tomography inspection revealed that melted copper had not penetrated in between the wires and instead created a mechanical joint. It resulted in a low

DOI: 10.13009/EUCASS2022-6196

measured thermal conductivity of 0.36 $W \cdot K^{-1}$, more than 4-times lower than required (Figure 3b). Additionally, the length of each individual wire was twice the height of the part and the heat was transferred along the wires rather than across the points where the wires were in contact [25].

2. Material and Methods

2.1 AlSi10Mg powder

The powder AlSi10Mg was produced by SLM Solutions Group AG, Lübeck, Germany using a gas atomization in nitrogen atmosphere. The morphology of similar powder was evaluated in the study of Vrána et al. [27] based on the scanning electron microscopy (Philips XL30 SEM, Amsterdam, The Netherlands) and showed almost a spherical shape of the particles. The powder particles had a large variability in size with a mean value of 41.4 μm and 90 % were up to 58.0 μm as investigated by the laser diffraction analysis (Horiba LA-960, Kyoto, Japan). Chemical composition defined by the vendor is shown in Table 1.

Table 1: Chemical composition (wt %) of SLM material AlSi10Mg [28]

Element	Si	Fe	Cu	Mn	Mg	Zn	Others	Al
SLM powder	9.0-11.0	0.55	0.05	0.45	0.20-0.45	0.10	0.45	Balance

Before the component fabrication started, the metal powder was dried to less than 5 % of residual humidity and subsequently filled into a recoater. All the samples were built on a platform (280 x 280 mm) made of aluminium alloy Al 3.3547 that was preheated to 150 °C. A 50 μm layer was applied corresponding to the particle size distribution.

2.1.1 Mechanical and thermal properties

The AlSi10Mg aluminium alloy metal powder was chosen over other materials due to its thermo-mechanical specific properties after artificial ageing. Different heat treatments were investigated by Vaverka et al. [29]. Two stage heat treatment - annealing and artificial ageing (T6: 520 °C/ 6 hours/ water quench/ 175 °C/ 4 hours) showed higher values of yield stress (YS) and on the contrary by 30 % lower ultimate tensile stress (UTS) compared to as-build.

Table 2: Mechanical properties after heat treatment – artificial ageing [29]

YS	***UTS***	***Elongation***	***R.S.****	***Thermal conductivity***
$R_{p0.2}$ [MPa]	R_m [MPa]	[%]	[MPa]	[$W \cdot m^{-1} \cdot K^{-1}$]
258	288	2.8	-17	163.1

* Compressive residual stress according to finite element (FE) analysis

2.1.2 Thermal conductivity analysis

Thermal conductivity was investigated for SLM fabricated and artificially aged samples 10x10x2 mm of AlSi10Mg alloy. Two main surfaces were polished and matted with graphite powder. Two samples were measured at the Institute of Plasma Physics, Czech Technology Agency (IPP-CAS) by a laser-flash method in vacuum (Linseis LFA 1000, Robbinsville, USA) with 5 measurements per sample. A deviation of measurements per one sample was ± 4 %. The samples were analysed by micro-computed tomography to reveal the porosity of 0.10 % at 10 μm resolution. The result of average 163.1 $W \cdot m^{-1} \cdot K^{-1}$ matches well the study of Sélo et al. [30] that refers to values of 145 ÷ 173 $W \cdot m^{-1} \cdot K^{-1}$ for samples heat treated by annealing.

2.2 Manufacturing and inspection

2.2.1 Selective laser melting

Additive production of both technology demonstrators was performed on an industrial 3D printer SLM 280HL (SLM Solutions Group AG, Lübeck, Germany) equipped with 400 W ytterbium fibre laser YLR-400-WC-Y11 (IPG Photonics, Oxford, USA) with a focus diameter of 82 μm and a Gaussian beam intensity distribution.

All parts were produced on two platforms under the process parameters (Figure 4c) developed to achieve a homogeneous component, low porosity and high productivity. Nitrogen gas flow was used during fabrication and the oxygen level was kept under 0.2 % threshold.

DOI: 10.13009/EUCASS2022-6196

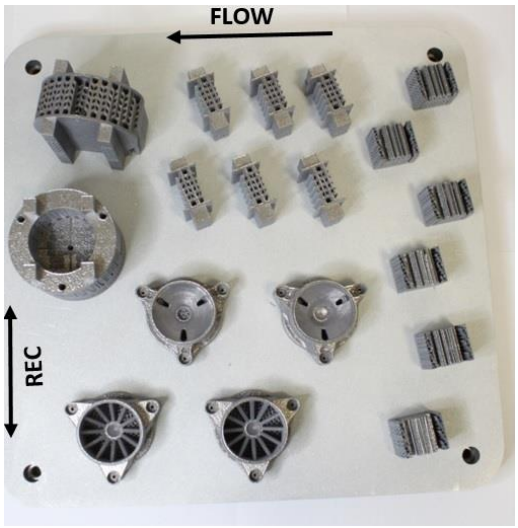

(a)

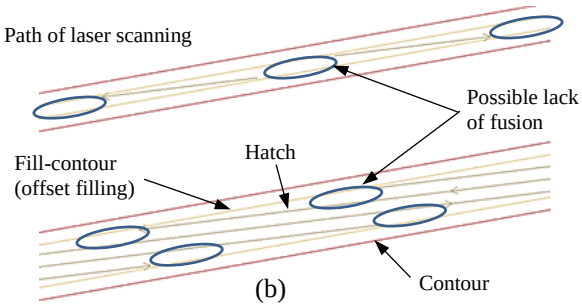

(b)

Laser power	350 W
Scanning speed – borders	500 mm·s^{-1}
Scanning speed – volume	930 mm·s^{-1}
Beam compensation	150 µm
Layer thickness	50 µm
Hatch distance	150 µm
Beam diameter	82 µm

(c) [27]

Figure 4: SLM manufacturing; (a) platform with Baseplate and Flexible thermal structure parts after SLM manufacturing; (b) two walls with different thickness - laser scanning strategy generated as default for thin wall structures; (c) SLM laser process parameters

The ‘’Offset filling’’ scanning strategy was used for the thin walls and support structures, Figure 4b. All parts were printed 5 mm above the platform on supports consisting of perforated blocks and cones. Support structures were generated to support surfaces with an inclination lower than 35° and with an area higher than 0.1 mm^2.

2.2.2 Porosity analysis

Internal porosity was analysed using a micro-computed tomography (µCT, GE phoenix v|tome|x L240, GE, Wunstorf, Germany). By each µCT measurement, two Baseplates, two Flexible structures or four thermal samples were jointly analysed. The linear voxel size resolution of 1/1000 of the largest sample size was 60 µm for the Baseplate and 75 µm for the Flexible structure. The post-processing of reconstructed data was performed in the software VGStudio MAX 3.1, including the porosity analysis module. In order to inspect the internal invisible surfaces of parts, scanned 3D data were also exported in STL format for dimensional and deformation analyses in GOM Inspect software.

2.2.3 Dimensional and deformation analysis

Visible surfaces of the Baseplate and Flexible structure were digitized by the optical 3D scanner Atos Triple Scan 8M (GOM GmbH, Braunschweig, Germany) with the optics MV170 to understand the deformations of parts in as-build and after artificial ageing. To successfully scan Al-alloy material that is highly reflective, parts were matted by $Ti0_2$ titanium powder with a thickness of 2 - 3 µm. The blue-light scanner resolution was then ± 0.005 mm. After the optical measurement, GOM Inspect software was used to analyse the dimensional deviations from 3D CAD model.

2.2.4 Post-processing of parts after SLM fabrication

After the production of SLM, all parts underwent a sequence of post-processes: de-powdering - inspection - heat treatment T6 - inspection - cut-off parts from platform - supports removal - inspection and surface treatment by sand blasting. Two inspections by the blue light 3D scanning were planned before & after heat treatment to evaluate the rising inaccuracies. The support structures were removed by a combination of Wire Electric Discharge Machining (Wire cut EDM, CHMER G32S, Taiwan) and manually. Subsequently, the parts were inspected by the micro-tomography to understand the precision of SLM production as well as the internal defects and invisible surfaces. The outer surfaces were treated by sandblasting (Suction Blast Cabinet SBC 420L with manual blast gun) to visually unify the parts. The direction of beam and time exposure was controlled manually by using abrasive of corundum particles.

2.3 Design of additive parts for heat switch

2.3.1 Baseplate design definition

The flatness of the Hot interface is essential to provide a contact surface for efficient heat transfer. Structural reinforcement encourages couple of design solutions, such as topology, parametric or multi-material optimization. The aim was to reach the best mass-to-stiffness ratio and to demonstrate the capabilities of conventional software tools and

DOI: 10.13009/EUCASS2022-6196

manufacturing processes. Based on the stiffness requirement (deflection < 0.02 mm), the height of the design domain was artificially increased by 5 mm compared to the former part, see dimensions in Figure 5.

2.3.2 Flexible thermal structure design definition

FTS mechanism, as part of the Miniaturized heat switch technology, represents the path of heat transfer. It shall be a thermally optimized structure with a specific thermal conductivity > 2.72 $W \cdot K^{-1} \cdot kg^{-1}$. The design space (Figure 6) was derived from the prior design with three cut-outs for pylons. Outer diameter was enlarged compared to the baseline design, taking into account the new additive technology application and a high thermal conductance requirement. The cross-section area of 1400 mm^2 was taken as the maximum size of the former heat switch [25].

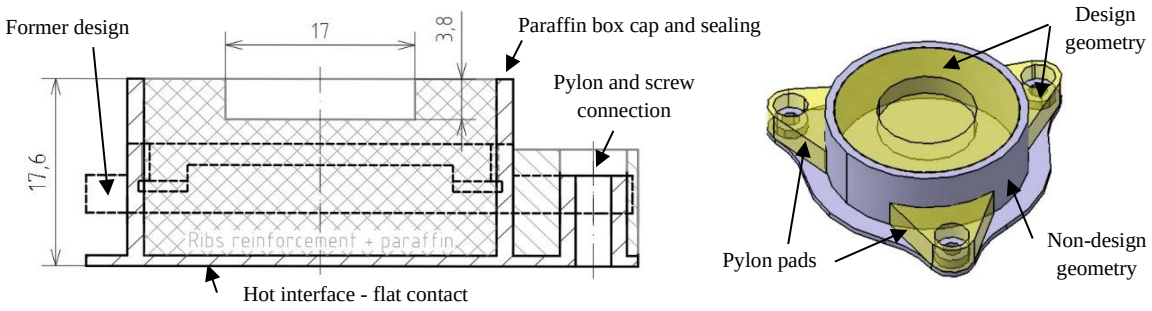

Figure 5: Baseplate non-design and design geometry (available for optimization); (a) BP baseline definition and comparison to former design (dimensions in millimetres); (b) ISO view of BP geometry

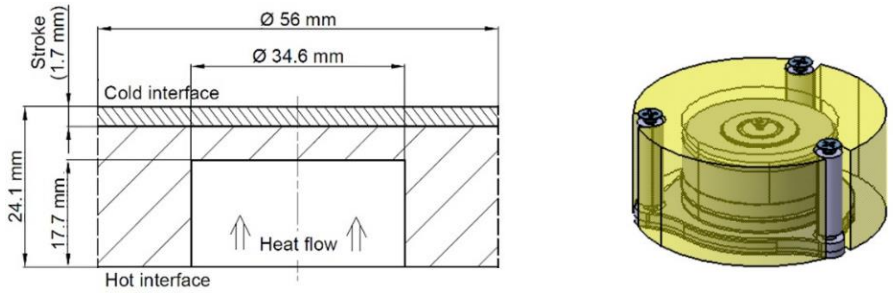

Figure 6: FTS design space available; (a) design space geometry cross-section [25]; (b) ISO view

2.4 FE numerical models

The topology optimization and finite element analysis (FEA) of the Baseplate were done using Tosca 2019 and Ansys 2019 R3. One sixth symmetry was used. The model contained the half of the pylon made from Torlon and simplified screw, all discretized by hexahedral elements C3D8R of 0.035 mm. Normal displacements were constrained to nodes on the planes of symmetry. The pressure of 16 MPa was applied to inner surfaces of the paraffin box. The nodes in upper surface of the Baseplate were tied with the reference point (Figure 7a) which enabled only vertical axial displacement. A reaction force was applied to the reference point in the axial direction and was equivalent to the distributed pressure load. The pylon, screw and base plate were connected with tie constraint. Material properties are listed in Table 3.

Objective function of the topology optimization was defined to minimize mass subjected to constraints for deformation (< 0.02 mm), maximum stress ($\sigma_{vonMises} \leq 110$ MPa) and manufacturability (minimum wall thickness 0.3 mm or 2.0 mm prescribed as minimum element size). Restriction of maximum vertical relative displacement d_z [mm] was prescribed for nodes on the Hot interface (Figure 7a) according to equation

$$-0.02 \text{ mm} < \Delta(d_{zmax} - d_{zmin}) < 0.02 \text{ mm}. \quad (1)$$

DOI: 10.13009/EUCASS2022-6196

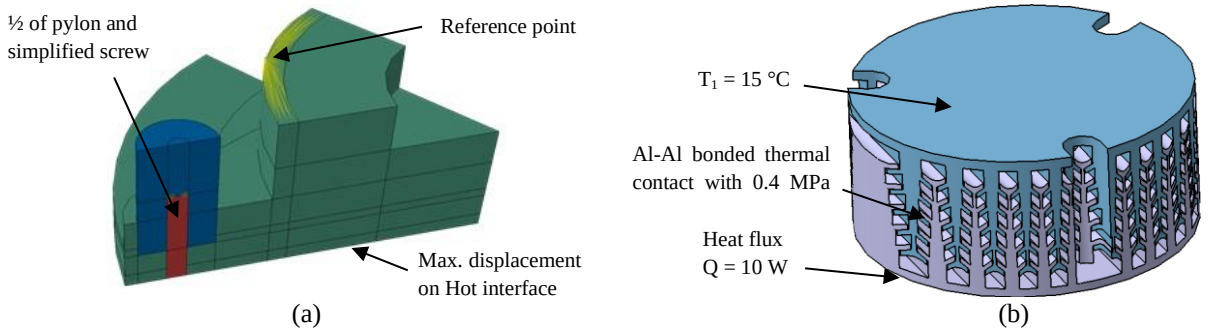

Figure 7: FE model set-up used for analyses and topology optimization; (a) BP boundary conditions; (b) FTS boundary conditions

Heat transfer analysis of the Flexible structure was carried out by Ansys 2019 R3 solver. Rough mesh consists of second order tetrahedral elements TET10 with element size 0.5 mm. Heat flux Q [W] is prescribed to one of the interfaces (10 W) and temperature (T_1 = 15 °C) is prescribed to the opposite interface. The average surface temperature (T_2) is used to calculate thermal conductivity q [W·K^{-1}] of the FTS structure from temperature difference according to equation

$$q = \frac{Q}{T_2 - T_1} \text{ [W·K}^{-1}\text{]}. \quad (2)$$

The thermal contact within the mechanism is set to bonded with surface heat transfer coefficient of 2127.9 W·m^{-2}·K^{-1} which equals to Al-Al contact of 0.4 MPa contact pressure and both surface roughness of Ra 1.6 µm. Heat leakage by radiation and convection was not considered.

Table 3: Material properties used in topology optimization and FEA analyses [28]

		AlSi10Mg (additive)	***Torlon 4203®***	***AISI 316L***
Thermal Conductivity	[W·m^{-1}·K^{-1}]	150	0.26	16
Density	[g·cm^{-3}]	2.69	1.42	7.8
Young´s Modulus	[GPa]	70.9	4.48	210
Poisson´s Ratio	[-]	0.33	0.45	0.27

3. Results

3.1 Baseplate Design

Multi-material design of Baseplate was successfully optimized, however was not to meet design requirements [26]. Therefore, out of many trials, three competitive designs were selected. Two geometry concepts are based on topology optimization with different restriction for minimum wall thickness 0.3 and 2.0 mm (Figure 8a,b) and one geometry is based on the conventional design of reinforcing ribs based on the designer's experience (Figure 8c).

To improve the stiffness of geometry BP(2) and BP(3), ISO grid (w/h 1:3) was designed with height of 1.5 mm and spacing 1.43 mm. The grid under 75° angle was limited by 1/6 symmetry and thus each line is not continuous in the neighbouring section. Generated ISO grid can be observed in Figure 8-1c (partially also in Figure 8-2,3b) and was identical for both aforementioned geometries. Design parameters of the ISO grid were not optimized.

3.1.1 Finite element analysis of Baseplate

Finite element analyses of the design concepts were performed taking into account its 1/6 symmetry (Table 4). BP(1) and BP(3) concepts meet the design requirement of deflection in vertical axis, whereas BP(2) reaches improvement by roughly 12 % due to the ISO grid and has stiffness lower by 50 % compared to the design target. Nevertheless, the geometry could be improved by the increased height of the ISO grid and by the application of reinforcement near the connection of the pylon pads to the vertical wall.

Analyses of fatigue life were performed but the stress concentrators were not suppressed, primarily for the uncertainty in the pre-selected paraffin pressure. Therefore, low-cycle-fatigue results are much lower than the required one hundred thousand. It corresponds to results of the static equivalent stress (von-Mises) that show strong concentrations of stress. More specifically, located at the edges of powder holes and in areas where small or none radius (fillet radius) exist.

DOI: 10.13009/EUCASS2022-6196

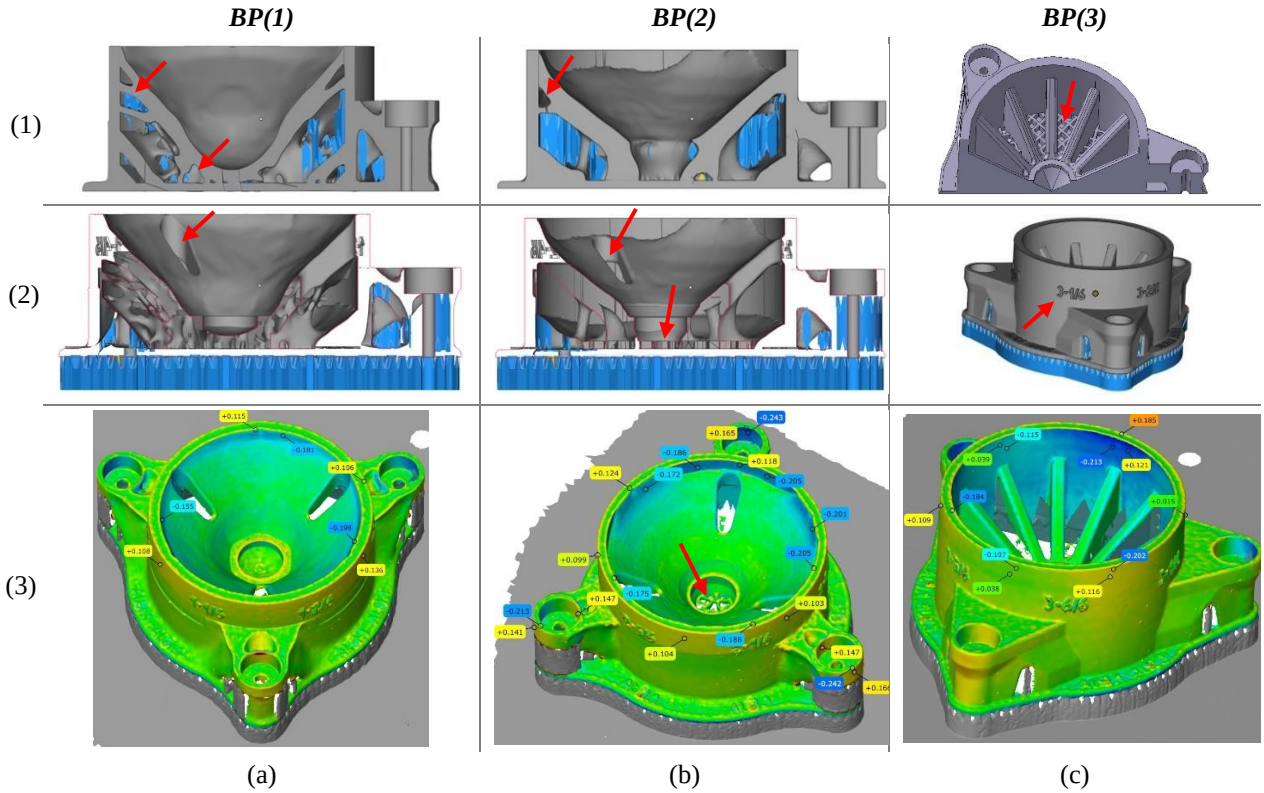

Figure 8: Three Baseplate competitive geometries (a) BP(1) topology optimized with min. wall thickness 0.3 mm; (b) BP(2) topology optimized with min. wall thickness 2.0 mm; (c) BP(3) with conventional design of reinforcing ribs; (1) supports structures default settings; (2) pre-print modifications and supressed internal supports; (3) optical 3D scan results after heat treatment – artificial ageing

Table 4: Results of Baseplate design concepts - FEA analyses overview

		BP(1)	***BP(2)***	***BP(3)***
Thermal Conductivity	[W·K^{-1}]	2.99	2.61	2.72
Weight	[g]	30.56	26.55	28.78
Deflection	[mm]	0.0166	0.0299	0.0192
Specific deflection	[mm·kg^{-1}]	0.543	1.126	0.667
Fatigue Life	[-]	1600	5500	25000

3.1.2 Baseplate design to be printed

Prior to the fabrication, geometry was modified for manufacturing constraints, eliminating closed cavities, too small features < 0.3 mm and surface angles < 35°. On the contrary, holes for powder removal, identification labels and support structures were added (red arrows in Figure 8-1,2). The holes for powder removal and paraffin filling were cut into a paraboloid wall in geometry BP(1) and BP(2); 3 holes per part, radially oriented in a location of pylon pads (Figure 8-2a,b). Analyses showed in this region lower loads and therefore also less reinforcement structure appears. The cut-outs for holes do not affect inner reinforcement and therefore do not decrease the mechanical properties of BP.

Based on the orientation of struts, walls and surfaces, the most promising orientation of 0° was selected to minimize the volume of supports needed. Generated supports solely inside the BP design are not removable by default (Figure 8-1a,b). Therefore, the primary aim for successful manufacturability was to supress the necessity of internal supports structures and avoid a powder locking inside the closed cavities.

3.2 Design of Flexible thermal structure

Out of many design concepts and optimization trials, a two-part mechanism design with 5 contact levels was selected (Figure 9). The design based on stems and branches in a “tree shape” with variable thickness is to meet the design requirements. All contact surfaces shall be in contact at the same time, which demands strict requirements for the

DOI: 10.13009/EUCASS2022-6196

additive manufacturing itself and the precision of the surface finishing operations. The higher the surface roughness, the higher is the thermal contact resistance and the lower the efficiency of the FTS mechanism. The build orientation has also a fundamental effect on the surface quality and manufacturability.

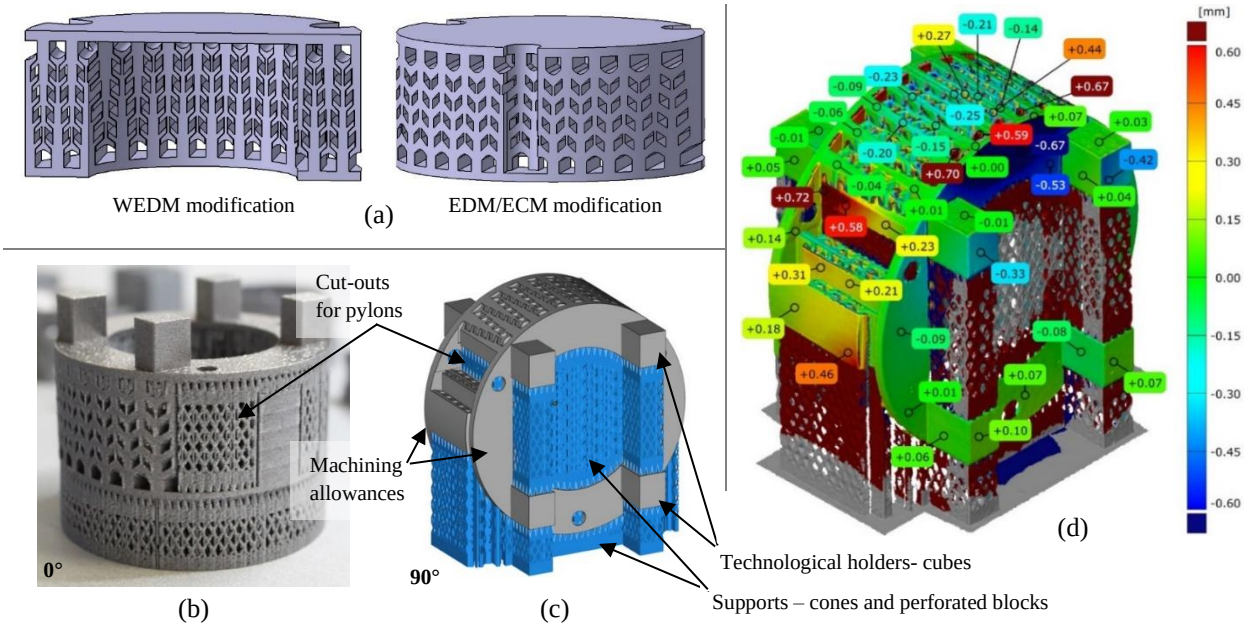

Figure 9: FTS mechanism; (a) FTS geometry modification according to surface treatment technology; (b) FTS(WEDM) in 0° orientation after SLM fabrication; (c) FTS(EDM) in 90° orientation – preparation of supports; (d) FTS(ECM) in 90° orientation after heat treatment – optical scanning results

3.2.1 Finite element analysis of FTS mechanism

Figure 10c shows, among others, the specific thermal ratio (thermal conductivity divided by weight) to meet the design target of 27.2 $W \cdot K^{-1} \cdot kg^{-1}$. Thermal conductivity and contact force were designed roughly 30 % higher than required however having negative impact on weight. The specific thermal ratio represents the key property of each FTS structure (i.e. of the distribution of material in horizontal and vertical direction within the design volume). Assuming that the specific parameter is constant and that the contact force and weight are directly proportional to the conductivity, the FEA results were recalculated with a target conductivity of 1.5 $W \cdot K^{-1}$. The parameters decreased by 27.9 % and are newly to meet the target values. The theoretical analytical calculation would be then converted to a real design modification by eliminating some thermal stem-branch structures. The specific thermal ratio is 10.3 % higher than required and might mitigate material and manufacturing uncertainties.

Additionally, a variable thickness of stems increases the overall part´s thermal conductivity by roughly 10.9 % by optimization of the heat flux while keeping the same weight, see Figure 10a,b. This effect was not included in the results of FEA presented in Figure 10c.

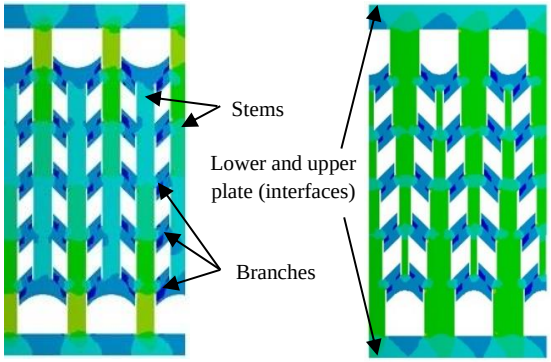

		FTS	*FTS (theoretical)*
Weight	[g]	69.26	49.98
Thermal conductivity	$[W \cdot K^{-1}]$	2.08	1.50
Specific Thermal Ratio	$[W \cdot K^{-1} \cdot kg^{-1}]$	30.01	30.01
Force*	[N]	1071.0	773.1

*To create 0.4 MPa contact pressure

(c)

Figure 10: FTS mechanism; (a) heat flux of FTS geometry cut-out; (b) optimized heat flux of FTS geometry cut-out with variable thickness of stems; (c) FEA results of Flexible structure

DOI: 10.13009/EUCASS2022-6196

3.2.2 Flexible structure design to be printed

To ensure that all 190 surfaces are at the same time in contact for efficient heat transfer, only three unconventional surface-finishing technologies were identified as applicable – Electrical Discharge Machining (EDM), Wire-EDM and Electro-Chemical Machining (ECM). However, each finishing technology demands its own specific geometry modification. The geometry for WEDM technology was printed as one part and subsequently was cut by the wire into two sections. On the contrary, for ECM and EDM technologies, the mechanism was printed as two parts 'assembled' together with a pre-defined clearance (Figure 9a). All manufacturing steps are leading to the same geometry at the end of the production cycle.

Four configurations of mechanism, WEDM modification in 0° and 90° (Figure 11e) orientations and EDM and ECM in 90° orientation (Figure 11d), were selected to assure manufacturability, removal of supports and surface treatment, while considering the position of all local surfaces. Despite the similar geometry, it was not possible to print the EDM and ECM configurations in 0° orientation due to the position of the branches in the upper part.

Prior to the fabrication, each geometry was modified for manufacturing constraints, adding machining allowances, support structures, technological holders-cubes, cut-outs for pylons and identification labels to assure fixation, clamping, easier machining and tracking of parts during all processes. Machining allowances were added to all contact surfaces to be subsequently machined (Figure 9b,c and 11e,f).

3.3 SLM manufacturing

Elements of concurrent design and manufacturing engineering were implemented to save time over the development cycle of parts [31]. Therefore, different geometry-based concepts of the Baseplate and manufacturability-based modifications of the Flexible structure were designed and subsequently manufactured by SLM. Production of parts (Figure 11) was roughly 8.5 hours per platform, consisting of 480 layers of the Baseplate and 882 or 1220 layers of the Flexible structure according to orientation.

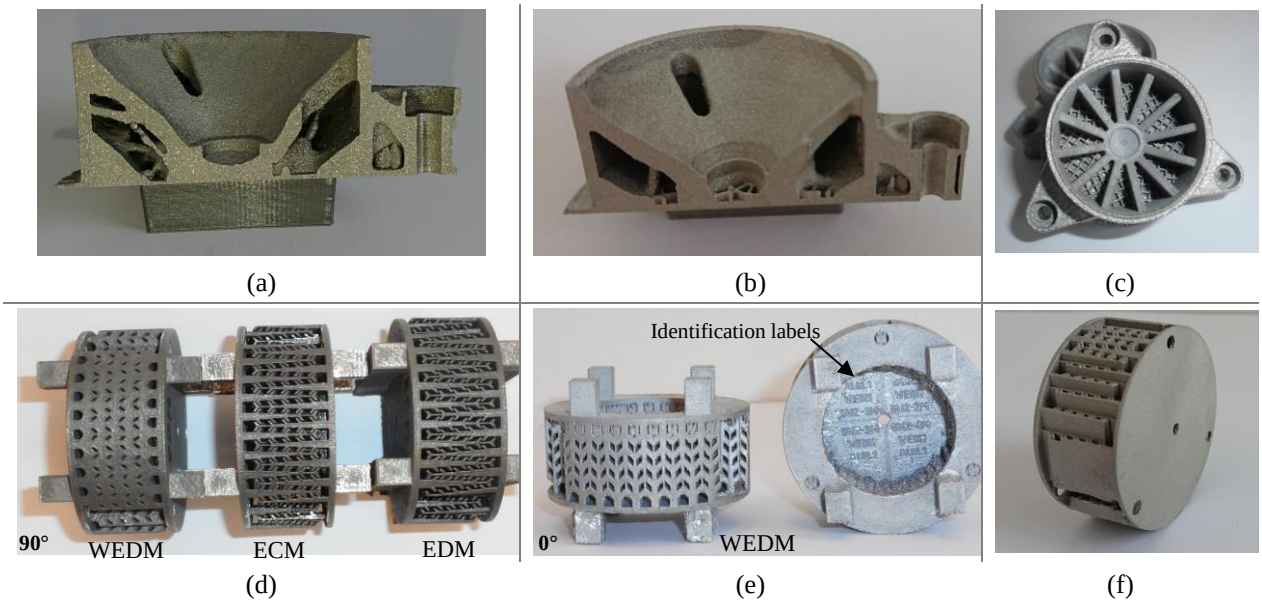

Figure 11: SLM manufactured parts; (a) BP(1) with 0.3 mm wall thickness constraint; (b) BP(2) with 2.0 mm wall thickness constraint; (c) BP(3) with ribs and ISO grid; (d) FTS build in 90° orientation in WEDM/EDM/ECM modification; (e) FTS build in 0° orientation in WEDM modification; (f) FTS after machining

3.4 Dimensional and porosity inspection

An overview of dimensional inaccuracy progression after the heat treatment is given in Table 5. Based on the 3D scanning of parts attached to the platform, majority of deviations in as-build are within ± 0.10 mm, while after the heat treatment larger deformations were measured mostly lower than ± 0.20 mm. However, the deviations in specific thin-wall locations reach up to ± 0.25 mm, as in Figure 8-3c. The part ECM (90°) apparently released strong residual stresses into an extensive deformation of the top-free end, up to + 0.19 mm in as-build and up to ± 0.70 mm after artificial ageing (Figure 9d). The effect is alike for all parts, but in smaller scale. No threshold was set-up for maximum deformation acceptance. No crack was observed.

DOI: 10.13009/EUCASS2022-6196

Table 5: Results of dimensional and porosity inspection

	Deformations *(accuracy ± 0.005 mm)*		***Porosity*** *(BP: 60 µm; FTS: 75 µm resolution)*	
	As-build	***Heat treated***	***Defect volumes***	***Porosity***
Baseplate	< ± 0.08 mm	< ± 0.20 mm, max. up to ± 0.25 mm	< 3 mm^3	< 0.025 %
Flexible structure	< ± 0.10 mm	< ± 0.20 mm, max. up to ± 0.70 mm	< 3 mm^3	≈ 0.01 %

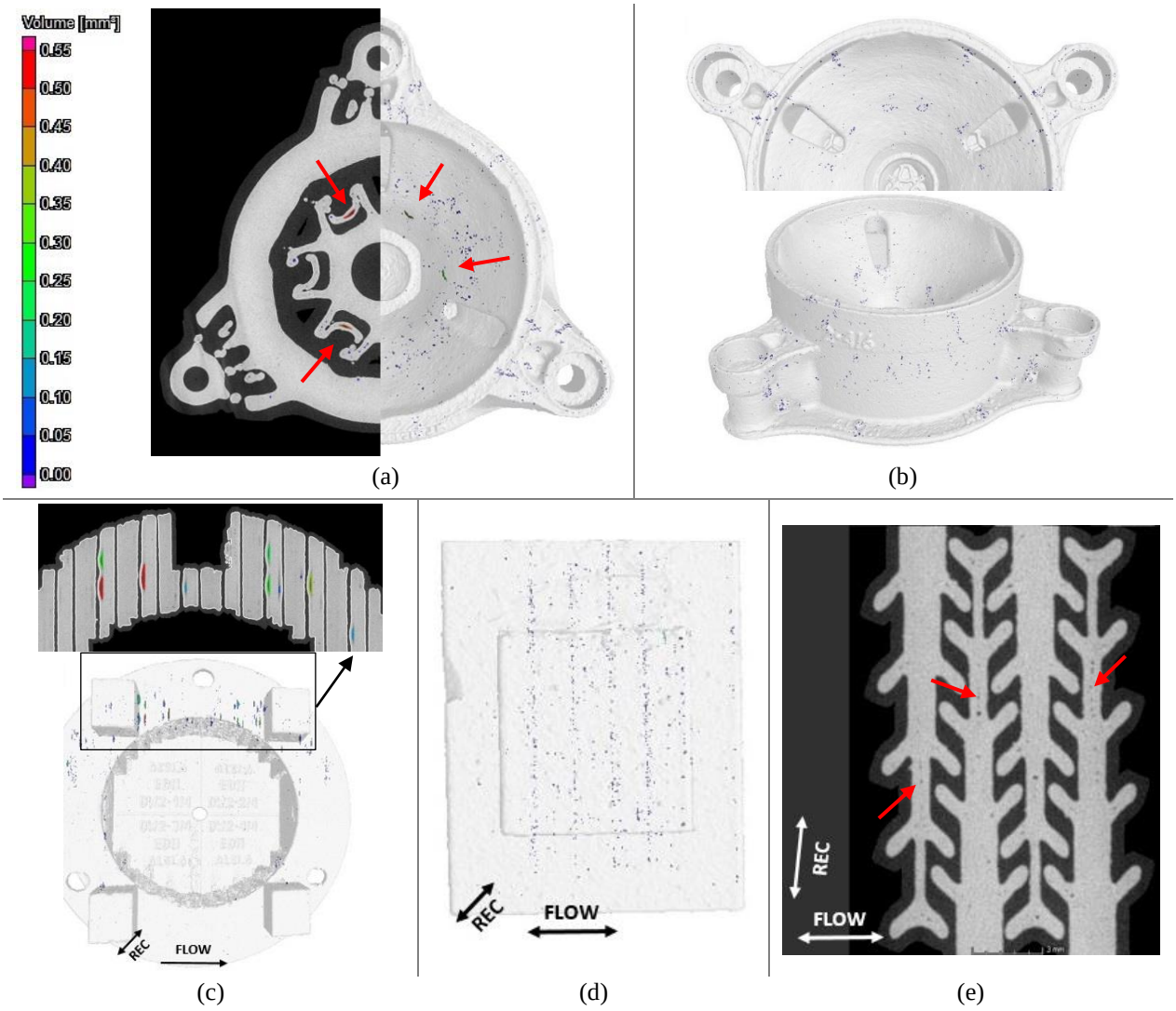

Figure 12: Micro-tomography evaluation of the FTS porosity; (a) BP(1) porosity distributed in pattern (defect layer 449); (b) BP(2) near spherical porosity; (c) FTS (EDM 90°) "lenticular" porosity in stems; (d) Cut-outs of FTS (EDM 90°) near spherical porosity distributed in parallel planes; (e) Cut-outs of FTS (EDM 90°) near spherical porosity distributed in the middle plane of each stem, particularly in wall-thickness of 0.65 mm

Micro-computed tomography scanning was performed for parts after supports removal (before surface machining) to inspect the invisible surfaces, hidden defects and porosity. Results of porosity evaluation can be seen in Table 5 showing small overall defect volumes, less than 3 mm^3 (BP parts < 0.025 % at resolution of 60 µm; FTS parts < 0.01 % at resolution of 75 µm). No acceptance threshold of porosity was defined.

Figure 12a,c show "lenticular" porosity and Figure 12b,d,e show tiny near spherical porosity, all distributed in patterns and symmetrical locations in the Baseplate as well as in the Flexible structure. In case of the FTS (EDM 90°), the "lenticular" porosity (Figure 12c) is located in the lower half of the FTS part which is connected by supports to the

DOI: 10.13009/EUCASS2022-6196

platform. In the upper free-end half, such porosity was not detected, however higher deformations occur due to the thermal stresses. The near spherical porosity (Figure 12d,e) appears in a region with higher distance between the laser scanning path of contour and fill-contour, as shown in Figure 4b. It was identified that for walls with thickness up to 0.7 mm only contours are scanned by laser. On the contrary, for wall with thickness higher than 0.8 mm also the fill-contour scanning is generated. If the wall thickness is around 0.7 mm (particularly 0.65 to 0.8 mm as measured) and the fill contour is not generated, the two contours are in the utmost distance and tends to be separated by porosity. Fortunately, this indicates the possibility to locally modify SLM process parameters or geometry to decrease such porosity appearance.

4. Discussion

4.1 Baseplate design maturity

The Baseplate (BP) design development study presented in the paper focused on the stiffness issue caused by paraffin pressure. Thus, several design concepts of the Baseplate were investigated, considering also multi-material additive design and manufacturing.

4.1.1 Design and optimization development

The design space was used for topology optimization to reach the best stiffness with the BP(1) concept (Figure 11a). The second approach to design stiffeners was the use of conventional rib reinforcement based on the designer´s experience. The BP(3) concept with ISO grid (Figure 11c) showed better weight-to-stiffness ratio (specific deflection as in Table 4) and generally was less sensitive to deviations in design boundary conditions and loads. Therefore, the use of parametric optimization of ribs and ISO grid (i.e. number, position, thickness) is considered for further research.

Generally, the topology optimization gives better mass distribution in terms of required stiffness however, in case of deviations in boundary conditions it shall be completely re-calculated. Alike, the topology optimization has higher sensitivity to manufacturing and processes deviations, has higher demands on CAD data, optimization software and their operators and gives much bigger challenge in post-processing operations to fulfil manufacturability and quality requirements. The most complex design of BP(1) (Figure 8a) demonstrates the current capabilities of software and manufacturing processes. Compared to the other presented concepts, it has better rate of paraffin melting (wetted area). On the contrary, all steps as designing, analyses, manufacturing, inspection and verification demand high precision and experience.

4.1.2 Multi-material

Multi-material design and optimization of the Baseplate was studied by local exchange of copper (as former material of the BP) with steel in order to decrease deformations. Firstly with the stiffness-based topology optimization by exchanging mesh elements, and secondly with the layer-wise topology optimization which better respects manufacturing possibilities [26]. In-house algorithm for customised topology optimization [32] was used for successful multi-material optimization of the BP design. However, preliminary analyses showed only negligible improvement in stiffness (only 15 % from roughly 0.3 mm to 0.25 mm compared to a single-material baseline) and predicted extensive problems with additive manufacturing [26]. The mismatch of coefficient of thermal expansion or metallurgy were not further investigated.

SLM manufacturing of multi-materials is of the latest interest with material change from layer to layer [33] or using multiple materials in one layer [34]. An interesting category is functionally graded material (FGM) [35] where one material gradually changes to another. It poses significant obstacles in terms of material compatibility and properties [36; 37], capabilities of additive 3D printers [33; 38] and specific process parameters for each material and their transition regions to prevent porosity, cracks, deformations and mutual segregation. Generally, studies show potential application of multi-material design [39] and metal multi-material manufacturing, but not yet ready for industrial use [40].

4.1.3 Additive and multi-objective optimization and software capabilities

Structural reinforcement encourages couple of design solutions, such as topology, parametric or multi-material optimization, implicating software challenges with additive constraints. At the time of project solution, conventional optimization software tools used as Nastran and Tosca supported only one restriction related to the additive manufacturing – minimum wall thickness. On the contrary, conventional software did not support multi-material or multi-objective optimization (e.g. thermal-stress) and majority of additive constraints, as the critical angle of overhanging surfaces and the effect of part orientation on manufacturability. Imitation of SLM production was only possible by conventional constraints of molding, forging or casting, defining a one-direction mass removal. However, such optimization results were not appropriate.

DOI: 10.13009/EUCASS2022-6196

4.1.4 Bio-inspired structures without supports

Produced Baseplate parts restricted the support structures to be generated inside of the paraffin compartment. Supports would not be possible to remove after manufacturing by any technology without degrading the geometry, surface or material itself. Higher roughness and powder stuck to the walls are expected on the internal surfaces, therefore the surface quality could be improved (treated by e.g. chemical etching).

The set of selected parameters for the additive (i.e. wall thickness, angle of non-supported overhanging surfaces and orientation of part) demonstrates the capability to meet design and manufacturing requirements and showed its potential applicability to the Heat switch technology. Machining allowances shall be added at the top free-end of the Baseplate to decrease thermal deformations. Micro-tomography showed relative density higher than 99.97 % that is in coherence with study of Kempen et al. [15]. Further, the parts will be verified by thermal-vacuum tests in the range of - 30 °C to + 60 °C and vacuum level up to 10^{-3} Pa [41].

4.2 Flexible thermal structure design maturity

4.2.1 Design development

The initial idea to eliminate problematic joints of the FTS assembly was to replace it by a single structure, thus eliminating all joining techniques. Therefore, topology optimizations with different set-up were performed to provide flexibility and mass reduction. However, results showed too low thermal conductivity (roughly 0.2 $W \cdot K^{-1}$), too high stresses (up to 250 MPa) and poor flexibility at the same time (≈ 0.3 mm stroke prolongation). Therefore, all single-structure concepts were considered not to be feasible and were rejected.

To design a new efficient Flexible thermal structure, analytical models were developed to compute thermal conductivity and weight. Verification by numerical analysis showed up to 10 % mismatch and confirmed the accuracy of the analytical calculation [25]. Therefore, optimization by analytical models was possible to increase both thermal conductivity and thermal specific ratio. Despite the higher thermal specific ratio with the increasing number of contact storeys, the maximum number of contact surfaces is limited to 5 due to the height of flexible structure. The FTS design development and optimization gave strict constraints of what is a feasible geometry to be printed.

4.2.2 Branch-stem mechanism with 190 surfaces in contact

The surface roughness in as-build condition is expected to be up to Ra 25 µm [21]. Regardless the build orientation, all contact surfaces shall be treated. Manufacturability was deeply studied based on the build orientation, the need of supports and the applicability of surface-finishing operations. The wire in WEDM and electrode in EDM technology reach the contact surfaces only in a straight direction. On the contrary, ECM technology might be applicable to any kind of geometry while using one part as anode and the other as cathode (no tool is needed).

Selected design and manufacturing parameters (i.e. wall thickness, supporting strategy and build orientation) led to a successful manufacturing without cracks. However, the top “free” ends (specifically in ECM and EDM design modification) showed high thermal deformations up to ± 0.70 mm after heat treatment, as noticeable in Figure 9d. Modifications shall be implemented to the selection of part orientation and supporting strategy, as it has strong impact on the overall deformations. Micro-tomography showed relative density higher than 99.98 % and similar defect volume of roughly 3 mm^3 as for the Baseplate.

4.3 Material, quality and inspection

AlSi10Mg is the most commonly SLM produced material from all aluminium alloys. It is easy to manufacture, heat treat and machine. There are many articles describing achievable microstructure, porosity, surface quality and their effects on tensile properties [23; 24]. On the contrary, aluminium alloys have fundamental drawbacks. Higher porosity up to 0.2 % [19], higher surface roughness up to Ra 25 µm [21] and geometry inaccuracy up to ± 0.3 mm due to thermal shrinkage and distortions [20] are the key aspects to understand and to set-up acceptable thresholds.

4.3.1 Material obsolescence and cold-welding phenomenon

AlSi10Mg alloy has very good corrosion resistance [28], however ageing and long term effects might cause material obsolescence. Moreover, data are missing for cold-welding effect that is an issue of the FTS mechanism, particularly in the impact load conditions. Fretting conditions might occur only during a lift-off if the switch is in ON mode. It is expected that the oxide layers created during the manufacturing would prevent such degradation. Al-based cubic fleet centred metals are generally more prone to adhesion due to the higher ductility. It is reported that the cold welding can be avoided by the use of dissimilar alloy pairs or by the coating application [42]. Theoretical predictions of this effect are not comparable with experimental data, therefore only testing is applicable.

DOI: 10.13009/EUCASS2022-6196

It was reported that hard-anodized Al-based alloys can withstand impact loads. Nevertheless, anodising is to degrade the thermal contact conductance and overall thermal efficiency of the FTS mechanism. The H_2SO_4 electrolyte galvanostatic anodizing was reported [43] to show significantly different anodizing behaviour when compared to the cast alloy. The process and resulting layer quality highly depends on substrate microstructure, selected heat treatment and voltage-time response. Moreover, the oxide layer growth is not symmetric [44].

4.3.2 Effect of defects and quality verification of complex parts

Additive development of the parts for heat switch showed a lack of automated evaluation of scanned data, to inspect complex parts as the bio-inspired tiny structures of the BP or roughly 190 contact surfaces of the FTS mechanism.

The effects of porosity (i.e. number, size, shape, distribution, location and interaction of pores) on mechanical properties shall be understood in respect to component design and loads. Du Plessis et. al. [22] investigated effects of defects for cylinder samples with induced porosity. It was reported that bigger and closer-to-surface pores tend to initiate crack growth leading to a break under quasi-static tensile loading. Other researches [45; 46] show the development of in-process SLM manufacturing real-time control to eliminate or appropriately modify porosity parameters. By a combination of both immature processes and supported by an extensive mechanical testing, inspection and numerical analyses, the thresholds and acceptance criteria could be determined for each additive part to be qualified for space application.

5. Conclusions

Current results of design, analyses, manufacturing and related issues were presented as well as some future steps in development towards possible future qualification. Broadly speaking, the BP and FTS parts readiness for space application is currently low. The presented outcomes are the 1st iteration of research and development for the heat switch technology that is continuously developed in parallel. The work done was to understand, analyse and verify the geometry concepts, their manufacturability, inspection procedures and dimensional precision – all to meet the requirements.

At the conclusion, we briefly review the knowledge gaps in the current state-of-the-art, such as software challenges with additive constraints, multi-material and multi-disciplinary optimization or lack of material data on surface treatment, material obsolescence and cold welding. Furthermore, we summarize issues related to the qualification of parts as the effect of defects and the manufacturing in-process control to mitigate cracks and porosity. All were also identified as major issues in our research. The presented outputs represent a successful demonstration of the capabilities, maturity and applicability of additive design and manufacturing. However, there are several future steps on the way to full qualification. It is estimated that the readiness of both additive parts was increased from TRL 2 to 3-4 within the project, under the supervision of ESA.

Acknowledgement

The research leading to these results was supported by the European Space Agency project “Additive Design for Aerospace Applications Capabilities”, Contract No. 4000123317/18/NL/GLC/hh.

I would like to express my gratitude to the colleagues Volodymyr Symonov M.Sc. and Ing. Jan Šplíchal, PhD., for cooperation and their professional assistance at the beginning of the project. My acknowledgement further belongs to all members of the ADAAC team.

References

[1] Peng, T., K. Kellens, R. Tang, Ch. Chen and G. Chen. 2018. Sustainability of additive manufacturing: An overview on its energy demand and environmental impact. *Additive manufacturing*. 21, 694-704. ISSN 2214-8604.

[2] Ngo, T. D., A. Kashani, G. Imbalzano, K. T.Q. Nguyen and D. Hui. 2018. Additive manufacturing (3D printing): A review of materials, methods, applications and challenges. *Composites. Part B, Engineering*. 143, 172-196. ISSN 1359-8368.

[3] Guessasma, S., W. Zhang, J. Zhu, S. Belhabib and H. Nouri. 2015. Challenges of additive manufacturing technologies from an optimisation perspective. *International Journal for Simulation and Multidisciplinary Design Optimization*. 6, 1-13. ISSN 17796288.

[4] Novak, K. S., C. J. Phillips, E. T. Sunada and G. M. Kinsella. 2015. Mars Exploration Rover Surface Mission Flight Thermal Performance. In: *SAE Technical paper series*. 35th International Conference on Environmental Systems (ICES), p. 14. ISSN 0148-7191.

DOI: 10.13009/EUCASS2022-6196

[5] Sunada, E., M. Pauken, K. Novak, C. Phillips, G. Birur and K. Lankford. 2002. Design and Flight Qualification of a Paraffin-Actuated Heat Switch for Mars Surface Applications. In: *SAE Technical Paper*. California Institute of Technology, p. 4. ISBN 10.4271/2002-01-2275.

[6] Guo, L., X. Zhang, Y. Huang, R. Hu and C. Liu. 2017. Thermal characterization of a new differential thermal expansion heat switch for space optical remote sensor. *Applied thermal engineering*. 113, 1242-1249. ISSN 1359-4311.

[7] Ando, M., K. Shinozaki, A. Okamoto, H. Sugita and T. Nohara. 2014. *Development of Mechanical Heat Switch for Future Space Missions*. 44th International Conference on Environmental Systems, p. 11. ISBN 978-0-692-38220-2.

[8] Krueger, H. 2017. Standardization for Additive Manufacturing in Aerospace. *Engineering*. 3(5), 585-585. ISSN 2095-8099.

[9] Frandsen, C. S., M. M. Nielsen, A. Chaudhuri, J. Jayaram and K. Govindan. 2020. In search for classification and selection of spare parts suitable for additive manufacturing: a literature review. *International journal of production research*. 58(4), 970-996. ISSN 0020-7543.

[10] Lasagni, F., J. Vilanova, A. Periñán, A. Zorrilla, S. Tudela and V. Gómez-Molinero. 2016. Getting confidence for flying additive manufactured hardware. *Progress in Additive Manufacturing*. 1(3-4), 129-139. ISSN 2363-9512.

[11] Allevi, G., M. Cibeca, R. Fioretti, R. Marsili, R. Montanini and G. Rossi. 2018. Qualification of additively manufactured aerospace brackets: A comparison between thermoelastic stress analysis and theoretical results. *Measurement: journal of the International Measurement Confederation*. 126, 252-258. ISSN 0263-2241.

[12] Boschetto, A., L. Bottini, M. Eugeni, V. Cardini, G. G. Nisi, F. Veniali and P. Gaudenzi. 2019. Selective Laser Melting of a 1U CubeSat structure. Design for Additive Manufacturing and assembly. *Acta astronautica*. .159, 377-384. ISSN 0094-5765.

[13] Addamo, G., O. A. Peverini, D. Manfredi, F. Calignano, F. Paonessa, G. Virone, R. Tascone and G. Dassano. 2018. Additive Manufacturing of Ka-Band Dual-Polarization Waveguide Components. *IEEE transactions on microwave theory and techniques*. 66(8), 3589-3596. ISSN 0018-9480.

[14] Szymanski, P. and D. Mikielewicz. 2022. Additive Manufacturing as a Solution to Challenges Associated with Heat Pipe Production. *Materials*. 15(4), 160. ISSN 1996-1944.

[15] Kempen, K., L. Thijs, J. Van Humbeeck and J.-P. Kruth. 2012. Mechanical Properties of AlSi10Mg Produced by Selective Laser Melting. *Physics procedia*. 39, 439-446. ISSN 1875-3892.

[16] Song, B., X. Zhao, S. Li, C. Han, Q. Wei, S. Wen, J. Liu and Y. Shi. 2015. Differences in microstructure and properties between selective laser melting and traditional manufacturing for fabrication of metal parts: A review. *Frontiers of Mechanical Engineering*. 10(2), 111-125. ISSN 2095-0233.

[17] O'Brien, M. J. 2019. Development and qualification of additively manufactured parts for space. *Optical engineering*. 58(1). ISSN 0091-3286.

[18] Dordlofva, C. 2020. A design for qualification framework for the development of additive manufacturing components-a case study from the space industry. *Aerospace*. 7(3), 25. ISSN 2226-4310.

[19] Aboulkhair, N. T., N. M. Everitt, I. Ashcroft and C. Tuck. 2014. Reducing porosity in AlSi10Mg parts processed by selective laser melting. *Additive manufacturing*. 1-4, 77-86. ISSN 2214-8604.

[20] Wang, D., Y. Yang, Z. Yi and X. Su. 2013. Research on the fabricating quality optimization of the overhanging surface in SLM process. *The International Journal of Advanced Manufacturing Technology*. 65(9), 1471-1484. ISSN 0268-3768.

[21] Strano, G., L. Hao, R. M. Everson and K. E. Evans. 2013. Surface roughness analysis, modelling and prediction in selective laser melting. *Journal of Materials Processing Technology*. 213(4), 589-597. ISSN 0924-0136.

[22] Du Plessis, A., I. Yadroitsava and I. Yadroitsev. 2020. Effects of defects on mechanical properties in metal additive manufacturing: A review focusing on X-ray tomography insights. *Materials & design*. 187. ISSN 0264-1275.

[23] Aboulkhair, N. T., I. Maskery, C. Tuck, I. Ashcroft and N. M. Everitt. 2016. The microstructure and mechanical properties of selectively laser melted AlSi10Mg: The effect of a conventional T6-like heat treatment. Materials science & engineering. A, *Structural materials: properties, microstructure and processing*. 667, 139-146. ISSN 0921-5093.

[24] Trevisan, F., F. Calignano, M. Lorusso et al. 2017. On the Selective Laser Melting (SLM) of the AlSi10Mg Alloy: Process, Microstructure, and Mechanical Properties. *Materials*. 10(1), p. 76.

[25] Černoch, J., J. Mašek and F. Löffelmann. 2022. Analytical and numerical analysis of thermal structure. In: *Engineering Mechanics 2022*. 27/28th international conference. p. 61-64. ISBN 978-80-86246-51-2. ISSN 1805-8256.

[26] Löffelmann, F. and J. Šplíchal. 2019. Design study of the heat switch base plate with single and multi-material topology optimization. In: *13th Research and Education in Aircraft Design: Conference proceedings*. p. 85-97. ISBN 978-80-214-5696-9.

DOI: 10.13009/EUCASS2022-6196

[27] Vrána, R., O. Červinek, P. Maňas, D. Koutný and D. Paloušek. 2018. Dynamic Loading of Lattice Structure Made by Selective Laser Melting-Numerical Model with Substitution of Geometrical Imperfections. *Materials*. 11(11). ISSN 1996-1944.

[28] SLM Solutions. 2021. Material Data Sheet: Al-Alloy AlSi10Mg. Lübeck, Germany: SLM Solutions Group AG, p. 5.

[29] Vaverka, O., D. Koutný, R. Vrána, L. Pantělejev and D. Paloušek. 2018. Effect of heat treatment on mechanical properties and residual stresses in additively manufactured parts. In: *Engineering Mechanics 2018*. p. 897-900. ISSN 1805-8256.

[30] Sélo, R. R. J., S. Catchpole-Smith, I. Maskery, I. Ashcroft and C. Tuck. 2020. On the thermal conductivity of AlSi10Mg and lattice structures made by laser powder bed fusion. *Additive manufacturing*. 34. ISSN 2214-8604.

[31] Ulu, E., R. Huang, L. B. Kara and K. S. Whitefoot. 2019. Concurrent Structure and Process Optimization for Minimum Cost Metal Additive Manufacturing. *Journal of mechanical design*. 141(6), 10. ISSN 1050-0472.

[32] Löffelmann, F. 2017. Failure Index Based Topology Optimization for Multiple Properties. In: *Engineering Mechanics 2017*. p. 590-593. ISBN: 978-80-214-5497-2. ISSN: 1805-8248.

[33] Wei, C., L. Li, X. Zhang and Y. Chueh. 2018. 3D printing of multiple metallic materials via modified selective laser melting. *CIRP annals*. 67(1), 245-248. ISSN 0007-8506.

[34] Chivel, Y. 2016. New Approach to Multi-material Processing in Selective Laser Melting. *Physics Procedia*. 83, 891-898. ISSN 1875-3892.

[35] Mahamood, R. M. and E. T. Akinlabi. *Functionally Graded Materials*. ISBN 9783319537559. ISSN 2364-3293.

[36] Sing, S. L., L. P. Lam, D. Q. Zhang, Z. H. Liu and C. K. Chua. 2015. Interfacial characterization of SLM parts in multi-material processing: Intermetallic phase formation between AlSi10Mg and C18400 copper alloy. *Materials characterization*. 107, 220-227. ISSN 1044-5803.

[37] Chen, J., Y. Yang, Ch. Song, M. Zhang, S. Wu and D. Wang. 2019. Interfacial microstructure and mechanical properties of 316L /CuSn10 multi-material bimetallic structure fabricated by selective laser melting. Materials science & engineering. A, *Structural materials: properties, microstructure and processing*. 752, 75-85. ISSN 0921-5093.

[38] Han, Z. and K. Wei. 2022. Multi-material topology optimization and additive manufacturing for metamaterials incorporating double negative indexes of Poisson's ratio and thermal expansion. *Additive manufacturing*. 54. ISSN 2214-8604.

[39] Yao, X.G., S. K. Moon, G. Bi and J. Wei. 2018. A multi-material part design framework in additive manufacturing. *International journal of advanced manufacturing technology*. 99(9-12), 2111-2119. ISSN 0268-3768.

[40] Wei, C. and L. Li. 2021. Recent progress and scientific challenges in multi-material additive manufacturing via laser-based powder bed fusion. *Virtual and physical prototyping*. 16(3), 347-371. ISSN 1745-2759.

[41] Mašek, J., D. Koutný and R. Popela. 2019. Thermal conductivity of Cu7.2Ni1.8Si1Cr copper alloy produced via SLM and ability of thin-wall structure fabrication. In: *13th Research and Education in Aircraft Design: Conference proceedings*. p. 119-129. ISBN 978-80-214-5696-9.

[42] Merstallinger, A., M. Sales, E. Semerad and B.D. Dunn. 2009. *ESA STM-279: Assessment of Cold Welding between Separable Contact Surfaces due to Impact and Fretting under Vacuum*. p. 66. ISBN 978-92-9221-900-6. ISSN 0379-4067.

[43] Revilla, R. I., D. Verkens, T. Rubben and I. De Graeve. 2020. Corrosion and Corrosion Protection of Additively Manufactured Aluminium Alloys-A Critical Review. *Materials*. 13(21), 25. ISSN 1996-1944.

[44] Leon, A., A. Shirizly and E. Aghion. 2016. Corrosion Behavior of AlSi10Mg Alloy Produced by Additive Manufacturing (AM) vs. Its Counterpart Gravity Cast Alloy. *Metals*. 6(7).

[45] Kruth, J.-P., P. Mercelis, J. Van Vaerenberg and T. Craeghs. *Feedback control of Selective Laser Melting*. Katholieke Universiteit Leuven, Department of Mechanical Engineering, Belgium, p.1-7.

[46] Mani, M., B. M. Lane, M. A. Donmez, S. C. Feng and S. P. Moylan. 2017. A review on measurement science needs for real-time control of additive manufacturing metal powder bed fusion processes. *International Journal of Production Research*. 55(5), 1400-1418. ISSN 0020-7543.

[47] Xia, L., Q. Xia, X. Huang and Y. M. Xie. 2016. Bi-directional Evolutionary Structural Optimization on Advanced Structures and Materials: A Comprehensive Review. *Archives of computational methods in engineering*. 25(2), 437-478 ISSN 1134-3060.

[48] Mašek, J. 2018. Thermo-Vacuum Test Chamber Development for Airborne and Space Equipment Testing in Simulated Extreme Conditions. In: *ICAS, 31st Congress of the International Council of the Aeronautical Sciences*. p.1-9.